

Exchange bias in reduced dimensions: Cobalt nanocluster arrays under the influence of nanometer thin MnPt capping layers

V. Sessi, S. Hertenberger, J. Zhang, D. Schmitz, S. Gsell, M. Schreck, R. Morel, A. Brenac, J. Honolka^{*}, and K. Kern

Citation: *Journal of Applied Physics* **113**, 123903 (2013); doi: 10.1063/1.4795274

View online: <http://dx.doi.org/10.1063/1.4795274>

View Table of Contents: <http://aip.scitation.org/toc/jap/113/12>

Published by the *American Institute of Physics*



Small Conferences. BIG Ideas.

Applied Physics
Reviews

SAVE THE DATE!
3D Bioprinting: Physical and Chemical Processes
May 2–3, 2017 • Winston Salem, NC, USA

The background of the banner features a stylized, glowing blue and red network of lines, resembling a biological or chemical structure, set against a dark blue background.

Exchange bias in reduced dimensions: Cobalt nanocluster arrays under the influence of nanometer thin MnPt capping layers

V. Sessi,¹ S. Hertenberger,² J. Zhang,² D. Schmitz,³ S. Gsell,⁴ M. Schreck,⁴ R. Morel,^{5,6} A. Brenac,^{5,6} J. Honolka,^{2,7,a)} and K. Kern²

¹European Synchrotron Radiation Facility, 6 rue Jules Horowitz, BP 220 38043 Grenoble Cedex 9, France

²Max-Planck-Institut für Festkörperforschung, Heisenbergstrasse 1, 70569 Stuttgart, Germany

³Helmholtz Zentrum Berlin für Materialien und Energie GmbH, Hahn-Meitner-Platz 1, 14109 Berlin, Germany

⁴Universität Augsburg, Universitätsstrasse 1, 86135 Augsburg, Germany

⁵Université Joseph Fourier, 17 rue des Martyrs, 38054 Grenoble, France

⁶INAC/SP2M, CEA, 17, rue des Martyrs, 38054 cedex 9 Grenoble, France

⁷Institute of Physics of the ASCR v. v. i., Na Slovance 2, 182 21 Prague, Czech Republic

(Received 15 January 2013; accepted 28 February 2013; published online 25 March 2013)

The magnetic behavior of cobalt nanocluster arrays arranged on a boron-nitride nanomesh and capped with MnPt layers of varying thickness θ_{MnPt} is investigated. The magnetic properties of the arrays are found to be strongly dependent on the cobalt nanocluster size: large 3-dimensional clusters of several nanometers size under the influence of only $\theta_{\text{MnPt}} \sim 5$ nm exhibit prototypical exchange bias behavior, whereas small 2-dimensional clusters of about 1 nm in diameter show superparamagnetic behavior, however, with a strong quenching of the average cobalt magnetization. The latter effect is correlated with the formation of a stable antiferromagnetic phase at increasing θ_{MnPt} and is discussed in terms of the domain state exchange bias model. The quenching suggests either partial antiferromagnetic alignment of cobalt spins within a cluster or a random orientation of cobalt cluster macrospins with respect to each other. © 2013 American Institute of Physics.

[<http://dx.doi.org/10.1063/1.4795274>]

I. INTRODUCTION

Exchange bias (EB) can appear when a ferromagnetic (FM) 3d metal like cobalt is brought in contact with an antiferromagnetic (AFM) material. The effect becomes manifest in a horizontal shift of the hysteresis curve by a characteristic field H_{EB} called exchange bias field. For a topical review, see Ref. 1. Phenomenologically, EB is known for decades, yet its microscopic origin is still under debate. H_{EB} has been initially attributed to an uncompensated magnetization in the antiferromagnet at the interface to the ferromagnet. However, in order to explain the manifold material and geometry dependent EB effects in the experimentally studied systems, more complex models had to be developed, taking into account defects, roughness, and the formation of magnetic domain walls at the interface (see Kiwi for an overview on EB theory²). A very recent theory is the domain state (DS) model,³ in which H_{EB} is correlated with the uncompensated bulk magnetic state of the antiferromagnet. In contrast to models focussing on disorder effects confined at the *interface*, here *volume* disorder plays the key role. Indeed, SQUID measurements in Ref. 4 convincingly support the DS model theory in the EB system of isolated Co nanoclusters immersed in a chemically disordered bulk MnPt matrix. Although the Mn interface magnetization that might develop close to the clusters is not directly measurable in SQUID magnetometry, the authors observe that the EB effect scales with a frozen, non-reversible bulk magnetization in the MnPt DS. The latter is modeled to depend on the blocking temperatures T_b^{MnPt} of the various AFM domains within MnPt.

The aim of the present work is to examine the same EB system but in reduced dimensions: Co nanocluster arrays on a surface capped with thin MnPt layers. To test the DS model, we first gradually reduce the size of the MnPt layer in order to drive the DS from the blocked ($T < T_b^{\text{MnPt}}$) to the unblocked ($T > T_b^{\text{MnPt}}$) regime, T being the measuring temperature. The latter regime naturally defines a dimensional limit for possible applications of such arrays. Second, we investigate the effect of Co-Mn magnetic interactions at the cluster-matrix interface also for smallest Co clusters in the superparamagnetic limit ($T > T_b^{\text{Co}}$), where a stable antiferromagnetic DS in MnPt prohibits overall ferromagnetic ordering of cobalt. A key of our work is the combination of SQUID and element selective X-ray magnetic circular dichroism (XMCD) techniques. In contrast to SQUID magnetometry used in Ref. 4, XMCD enables the magnetic characterization of Co and Mn independently. The work is along the line of recent investigations on limits in size of exchange biased magnetic entities, like, e.g., single molecule magnets.⁶

The manuscript is organized as follows: After a short description of the sample preparation procedures and the experimental methods (Sec. II), in Sec. III the results are presented and discussed separately for the case of large 3-dimensional Co nanoclusters (Sec. III A) and small 2-dimensional clusters (Sec. III B). Finally, a qualitative model is proposed to explain the correlation between Co and Mn magnetic properties in the latter system.

II. MATERIALS AND METHODS

The samples were prepared in UHV conditions and then transported in air to BESSY II (high-field endstation,

^{a)}Electronic address: j.honolka@fkf.mpg.de

beamline UE46-PGM1) and to ESRF (beamline ID08) for XMCD measurements. Insulating boron nitride (BN) layers on Rh(111) surfaces were prepared using standard UHV procedures. Rh(111) single crystal and epitaxial Rh thin films (50–200 nm) grown on YSZ/Si(111) wafers were used as substrates. YSZ/Si(111) wafer fabrication involved pulsed laser deposition (PLD) for the oxide buffer and a two step e-beam evaporation procedure for the epitaxial metal film.⁹ Surfaces were cleaned with cycles of sputtering at 1.5 keV and 0.8 keV (Rh(111) and Rh/YSZ/Si(111), respectively), and annealing to 1250 K. The boron-nitride layer was formed by thermal decomposition of borazine gas, ($B_3N_3H_6$), while the Rh(111) surfaces were kept at 1250 K.⁷ The resulting h-BN layers are atomically thin, electrically insulating, chemically inert, and mechanically extremely stable. They show a strain-driven hexagonally ordered corrugation with a periodicity of 3.2 nm.^{8,10}

The first set of samples with large Co clusters situated on h-BN was prepared using a sputtering gas-aggregation source at CEA in Grenoble.³⁵ The h-BN substrates were prepared at the Max-Planck Institute in Stuttgart and annealed once more *in-situ* at the CEA under UHV conditions to assure clean substrate surfaces before cluster deposition. Spherical Co clusters with 4.5 nm average diameter (see Fig. 1(b)) were deposited on the substrate at room temperature and subsequently capped by variable coverages of MnPt sputtered from targets. The sample was terminated by a protective 5 nm thick Pt layer.

The second set of samples with small Co clusters was instead prepared by 3 subsequent buffer layer assisted growth (BLAG) cycles on the h-BN (see Fig. 1(a)). During each BLAG cycle, a Xenon buffer layer of 5 Langmuir thickness was prepared at low temperatures followed by the deposition of 0.05ML cobalt and annealing at 300 K (see Ref. 18 for details). After that, several capping materials, both non-magnetic (Au, Pt, Al_2O_3) and magnetic (MnPt), were

deposited *in-situ* by means of evaporators pre-calibrated by a quartz balance. The capping layers here were between 1 nm and 3 nm, depending on the sample. In the case of MnPt capping, during the co-deposition a blind was moved across the sample surface, resulting in a staircase MnPt wedge. The sample was again terminated with a 2 nm Pt protective layer. Mn/Pt ratio and quality of the wedge were verified using Auger spectroscopy. The sample structure has been checked also by means of TEM measurements. The supporting Rh substrate was found to be single crystalline, whereas the Pt capping is polycrystalline (see Fig. 1(c)). The formation of this polycrystalline structure is due to nucleation and growth on the corrugated h-BN which for room temperature deposition of 3d and 5d metals leads to formation of 5–10 nm sized 3-dimensional grains.³⁴

X-ray absorption spectroscopy (XAS) measurements were performed in the total electron yield (TEY) mode with 100% and 90% circularly polarized synchrotron light at ESRF and BESSY II, respectively. XMCD spectra were obtained at the $L_{3,2}$ absorption edges of Co and Mn as the difference between XAS spectra corresponding to right (σ^+) and left (σ^-) circularly polarized light. A collinear external magnetic field induces a sample magnetization along the x-ray beam, while the sample orientation was varied between the polar geometry ($\vartheta = 0^\circ$, sample normal parallel to the field) and the in-plane geometry ($\vartheta = 70^\circ$, sample normal and field enclose an angle of 70°). XMCD spectra are evaluated by normalizing the peak amplitude at the L_3 absorption edge by the corresponding non-dichroic XAS peak amplitude, in the following referred to as the XMCD/XAS ratio $R_{L_3} = \frac{(\sigma^+ - \sigma^-)}{1/2 \cdot (\sigma^+ + \sigma^-)}|_{L_3}$. Although the detailed shape of the $L_{3,2}$ XMCD spectra is a complex superposition of ground state expectation value contributions of the spin, orbital and spin-dipole operator,¹⁹ in bulk-like materials (e.g., large Co clusters, first set of samples) the ratio R_{L_3} is a good measure of the average spin moment $\langle \mu_S \rangle$ per atom, since here orbital (L_z) and spin-dipole operator (T_z) contributions can be considered as small. However, in reduced dimensions like monolayer islands of cobalt (second set of samples)—especially when in contact with heavy metal surfaces like, e.g., Au or Pt— T_z contributions can be significant and corrections to the value R_{L_3} have to be taken into account.²⁰ Element selective magnetization versus magnetic field curves are obtained by recording the field dependence of the XAS intensity at the cobalt and manganese L_3 absorption edge and normalizing the results to the respective XAS intensity at the L_3 pre-edge.¹¹

III. RESULTS

A. Large deposited clusters: Classical exchange bias regime

We have investigated samples with several MnPt coverages $\theta_{MnPt} = 5, 20, \text{ and } 80 \text{ nm}$. The effective thickness θ_{Co} of the deposited Co clusters estimated from microbalance and SQUID is about $(0.5 \pm 0.2) \text{ nm}$. With 4.5 nm diameter clusters, the areal substrate coverage is then close to 10%. A reference sample using a plane Si wafer as a substrate instead of the h-BN was also investigated, to compare the cluster

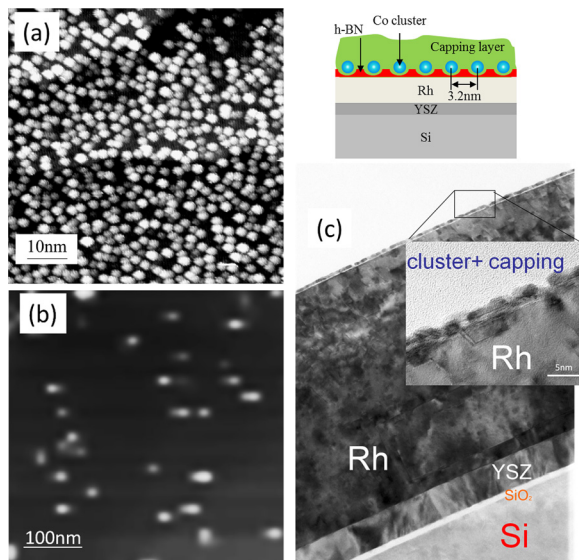


FIG. 1. Scanning tunneling microscopy of BLAG (a) and atomic force microscopy of deposited (b) clusters on the h-BN before deposition of the capping layer; sketch of the general sample structure and TEM image of a BLAG sample capped with Pt (c).

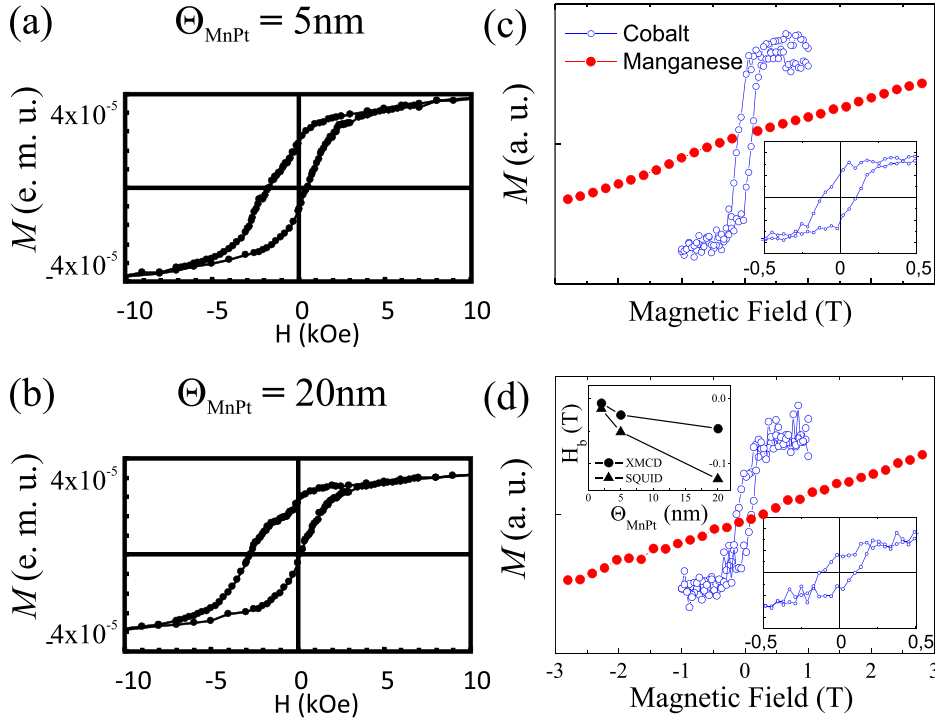


FIG. 2. Magnetization curves after in-plane FC at $\vartheta = 90^\circ$ with $H = +30$ kOe measured by SQUID (a)-(b) and XMCD (c)-(d) for Co and Mn at the two indicated MnPt coverages. The insets in (c) and (d) are close up views of the Co hysteresis. The additional inset in (d) shows H_{EB} as a function of θ_{MnPt} .

properties. On both substrates h-BN and Si, the cluster density is about $150 \text{ cluster}/\mu\text{m}^2$. Little aggregation between clusters is found, on both substrates. An atomic force microscopy image of the clusters on the h-BN before capping is shown in Fig. 1(b). The clusters contain an average of 4000 atoms and show a multiply twinned fcc icosahedral structure.³⁵

Magnetization curves shown in Fig. 2 were recorded both by SQUID and XMCD after field cooling (FC) from room temperature to $T = 6\text{--}8$ K with $H = +30$ kOe applied in-plane ($\vartheta = 90^\circ$). Table I summarizes the magnetic properties of the different systems, as measured by SQUID and XMCD. The blocking temperature T_b^{Co} of the cobalt clusters is given by the maximum in the zero field cooling magnetic susceptibility curves measured at 100 Oe (not shown here). We find values T_b^{Co} in the range of 80–130 K, well above the SQUID and XMCD measuring temperatures, a prerequisite for EB.

SQUID loops in Figs. 2(a) and 2(b) were measured at $T = 6$ K, with the magnetic field fully in the plane of the sample surface, according to the FC procedure. The data prove that indeed for all MnPt coverages the system behaves like a prototypical EB system, that is (i) the clusters show hysteresis

and (ii) EB is found for all the investigated samples. Both H_{EB} and T_b^{Co} increase with the MnPt thickness. A small vertical offset in the SQUID data due to uncompensated MnPt magnetization is present in samples with $\theta_{MnPt} = 80$ nm (not shown), indicative for the presence of a frozen, non-reversible magnetization in the MnPt. For thinner MnPt capping, this offset cannot be further resolved. The observed offset corresponds to an average Mn moment of $\sim 1 \times 10^{-3} \mu_B$ in the AFM matrix and it is similar to what is reported by Morel *et al.*⁴ for comparable systems. It suggests the formation of a partly blocked DS ($T_b^{MnPt} > 8$ K) in the diluted AFM matrix during FC.

The element specific response to the external magnetic field is accessible via XMCD presented in Figs. 2(c) and 2(d). Magnetization curves are shown separately for Co and Mn for the two indicated coverages $\theta_{MnPt} = 5$ nm and 20 nm. Due to the mean free path of electrons limiting the probed depth in the TEY mode, the Co signal in the 20 nm sample could only be investigated by fluorescence yield (FY). Cobalt magnetization curves display hysteresis with a coercivity similar to what is observed by SQUID, and a slight EB effect, which increases with the MnPt coverage (see inset of Fig. 2(d)). The EB field is reduced compared to what is seen by SQUID, partly because the magnetic field during in-plane XMCD measurements ($\vartheta = 70^\circ$) is 20° away from the field direction during FC. For all the samples, the Mn magnetization appears as a straight line without vertical shift, a consequence of the highly compensated AFM phase in MnPt as we will discuss further below.

Cobalt (a) and manganese (b) XAS and XMCD spectra at $\vartheta = 70^\circ$ are shown in Fig. 3 for the sample with $\theta_{MnPt} = 20$ nm under a magnetic field $B = 5$ T. In Figs. 3(c) and 3(d), we report the corresponding values of the ratio R_{L3} (see definition in Sec. II) versus θ_{MnPt} for both geometries $\vartheta = 0^\circ, 70^\circ$. From Fig. 3(c), it is evident that the Co

TABLE I. Summary of the SQUID and XMCD results for deposited cluster samples capped with different MnPt thicknesses θ_{MnPt} : EB field (H_{EB}), blocking temperature (T_b^{Co}), and orbital-spin moment ratio ($\frac{\mu_L}{\mu_S + 7\mu_T}$) are reported.

Substrate	θ_{Co} (nm)	θ_{MnPt} (nm)	H_{EB} (Oe)	T_b^{Co} (K)	$\frac{\mu_L}{\mu_S + 7\mu_T}$ In-plane	Polar
Si	0.4	80	2203			
Si	0.5	20	1326	110	(0.11 ± 0.02)	(0.09 ± 0.02)
h-BN	0.5	20	1233	130	(0.11 ± 0.02)	(0.08 ± 0.02)
h-BN	0.5	5	513	120		

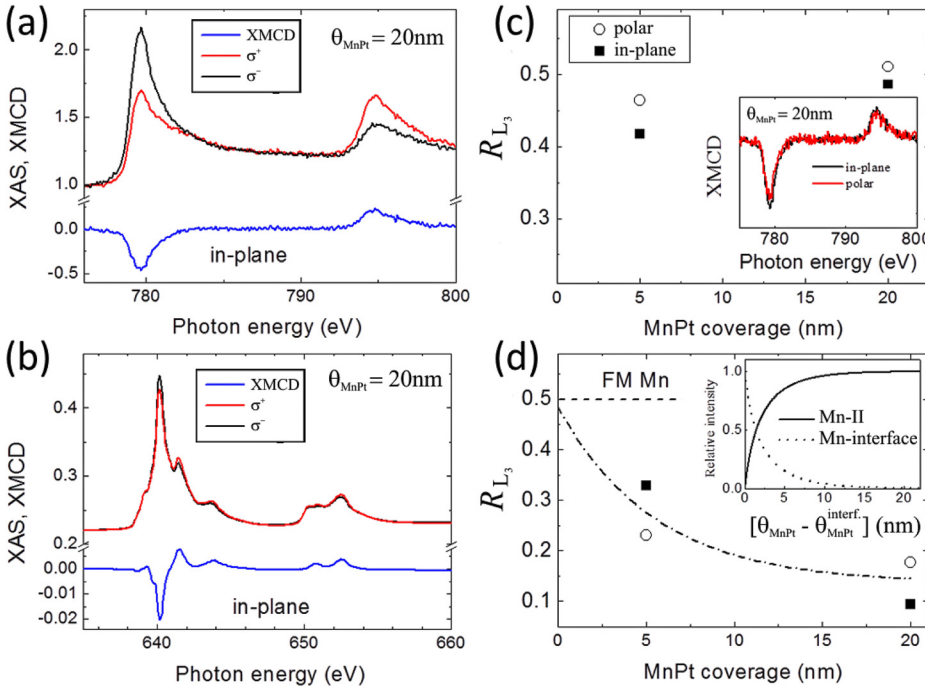


FIG. 3. Cobalt (a) and manganese (b) XAS (σ^+ , σ^-) and XMCD spectra at $\vartheta = 70^\circ$, $B = 5$ T, and $T = 8$ K for $\theta_{\text{MnPt}} = 20$ nm. The Co signal has been measured in FY and the Mn signal in TEY. $R_{L_3}(B = 5$ T) versus MnPt coverage are shown for Co (c) and Mn (d) both at $\vartheta = 70^\circ$ (filled symbols) and $\vartheta = 0^\circ$ (open symbols). A guide to the eye is added in (d) (dashed-dotted line). The inset in (c) contains the Co XMCD at $\theta_{\text{MnPt}} = 20$ nm for $\vartheta = 0^\circ, 70^\circ$ geometries scaled at the L_2 absorption edge. The inset in (d) shows the attenuation of the XAS intensity of Mn atoms close to the cluster surface due to the limited electron escape depth.

magnetization is slightly higher at $\theta_{\text{MnPt}} = 20$ nm, which can be attributed to the onset of oxidation effects at $\theta_{\text{MnPt}} = 5$ nm (Comment: For θ_{MnPt} of only 2 nm, the partial oxidation is clearly visible in the XAS spectral shape, data not shown). It seems that when the layer thickness becomes comparable to the cluster size, protection against formation of an oxidized AFM phase is strongly reduced. As we can see in Fig. 3(a) instead, for larger MnPt coverages the XAS and XMCD of Co display a typical metallic spectral shape and the value $R_{L_3} \sim 0.5$ is similar to what is found in FM bulk Co,¹² where values between 0.5 and 0.6 are reported. Since the clusters are bulk-like we can assume R_{L_3} to reflect the bulk Co spin moment (see comment in Sec. II) of $\mu_S \sim 1.6\mu_B$. We observe that (i) the magnetization is quite isotropic as no strong differences are found for R_{L_3} between $\vartheta = 0^\circ$ and 70° and (ii) there is little orbital moment anisotropy. The latter is visible in the inset of Fig. 3(c) where the XMCD spectra $\vartheta = 0^\circ$ and 70° are scaled to each other at the L_2 absorption edge. An anisotropy in the orbital moment would lead to different intensities at the L_3 edge in this plot. In general, the orbital moment is quenched, as one can also see from the small orbital-spin ratio (0.11 ± 0.02) in Table I, which is comparable to what is found for bulk cobalt.¹²

In Fig. 4(a), we report the Mn $L_{3,2}$ XAS signals at $\vartheta = 0^\circ$ and 70° for the investigated samples. In addition, XAS spectra simulated with the CTM4XAS software¹⁴ are shown for Mn(2^+) in O_h crystal fields with $10Dq = 0.6$ eV. For $\theta_{\text{MnPt}} = 20$ and 5 nm, the $\vartheta = 70^\circ$ XAS signal is well reproduced by the simulated curve. At $\vartheta = 0^\circ$, instead smoother spectra are found, similar to what is reported in Ref. 15 for an 8 ML thick MnPt film displaying the ordered $L1_0$ phase with the c -axis along the surface normal. The anisotropic growth conditions due to the contact with the h-BN/Rh(111) surface seem to induce a partly oriented $L1_0$ phase also in our samples.

We move now to the interpretation of the Mn XMCD data in Fig. 3(d). As already mentioned for $\theta_{\text{MnPt}} = 20$ nm,

the Co signal is not visible in TEY since the escape depth of electrons λ_e in the MnPt plus Pt matrix is ≤ 50 Å. By TEY, we thus observe the manganese signal from a bulk MnPt volume far away from the cluster or the h-BN substrate interfaces, which we call Mn-II hereafter. This effect is illustrated in the inset of Fig. 3(d) where the yield arising from Mn atoms at the cluster interface is plotted versus MnPt coverage.¹³ In the sample with $\theta_{\text{MnPt}} = 5$ nm, we are more sensitive to Mn atoms situated close to the Co cluster interfaces. The fact that we do not observe hysteresis in the Mn magnetization curves measured by XMCD, however, proves that the fraction of Mn atoms which follow the Co magnetization is small compared to the total amount of Mn. Here, we want to

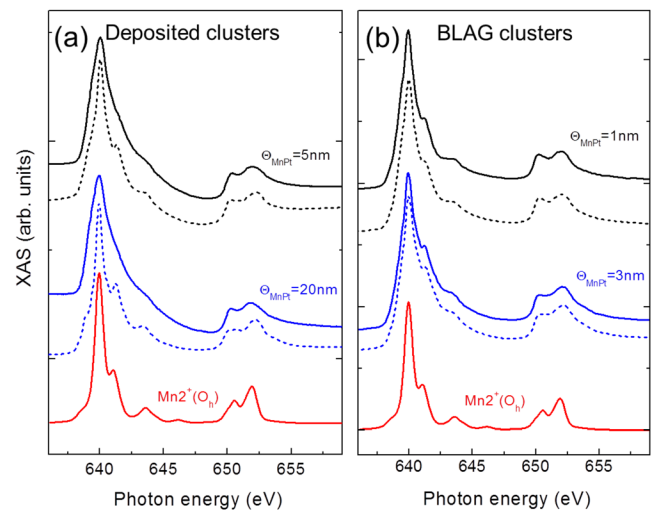


FIG. 4. Mn $L_{3,2}$ XAS for $\vartheta = 70^\circ$ (dotted lines) and $\vartheta = 0^\circ$ (continuous lines) at different coverages θ_{MnPt} for deposited clusters (a) and BLAG clusters (b). The curves have been multiplied by an arbitrary factor and shifted vertically for reasons of clarity. For comparison, XAS spectra of O_h crystal field simulations are shown in red at the bottom. Details about simulations are given in the text.

stress that the areal density of clusters covering the h-BN is low (see Fig. 1(b)), which generally reduces the fraction of Mn atoms at the interface with Co. For similar reasons, it is also not surprising that we do not resolve the small non-reversible vertical shift visible in our SQUID magnetization curves (corresponding to an average moment per Mn atom $\leq 1 \times 10^{-3} \mu_B$), which according to the DS model is indicative of EB.

With the above considerations, we can explain the decrease of the Mn R_{L_3} signal between 5 nm ($R_{L_3} \sim 0.3$) and 20 nm ($R_{L_3} \sim 0.15$) of MnPt (both signals significantly smaller than those found for FM aligned Mn spins in MnPt₃ with $R_{L_3} \sim 0.5$ (Ref. 29)). The first and most obvious explanation is that the formation of a long-range ordered AFM phase, in general, requires a minimum thickness of at least 6–10 nm.^{28,30} Another explanation, however, would emphasize the importance of structural disorder. Due to structural disorder visible in our TEM images, it can be expected that non-compensated spins are present in the MnPt matrix, similar to, for example, at the surface of CoO films.^{32,33} Therefore, larger Mn R_{L_3} values found for the $\theta_{\text{MnPt}} = 5$ nm sample compared to the $\theta_{\text{MnPt}} = 20$ nm sample can also partly be due to increased disorder and thus smaller grain sizes in the thin film regime. Indeed, during the sputter deposition of MnPt at room temperature the pits of the h-BN nanomesh are known to serve as a template for cluster nucleation which limits the grain size.¹⁶ With increasing coverage, we expect less corrugation, larger grain sizes, and thus more compensated spin structures. This more ordered magnetic phase with larger domains should correspond to the regime of the bulk DS model.

To summarize, we observe the classical EB behavior in FC systems of magnetically blocked ($T < T_b^{\text{Co}}$) cobalt nanoclusters on h-BN capped with MnPt layer thicknesses from 80 nm to as low as 5 nm. The Mn magnetization visible in the element selective XMCD technique proves a paramagnetic behavior and an increasingly compensated phase in the MnPt layers with larger capping layer thicknesses. We interpret the observed increasing EB field with increasing MnPt thickness as the progressive stabilization of a frozen, non-reversible MnPt magnetization due to blocking in enlarged DS units ($T < T_b^{\text{MnPt}}$) according to the DS model.

B. Small BLAG clusters: Superparamagnetic regime

Nanocluster formation during BLAG is a phenomenon extensively investigated in previous works.¹⁸ In particular, it can be exploited to build highly ordered arrays of Co nanoclusters on a patterned template substrate, as in the case of the h-BN nanomesh on Rh(111). Due to the template effect of the hexagonally corrugated structure of h-BN, a dense array of well-separated Co clusters of monatomic height and about 2 nm in diameter is formed (see Fig. 1(a)). A summary of the magnetic properties of BLAG nanoclusters discussed in Sec. III B can be found in Table II.

1. Non-magnetic capping

At first, three different capping materials Au, Pt, and Al₂O₃ were used to study possible influences of non-magnetic origin on the BLAG cluster properties.

TABLE II. Summary of the Co XMCD results for BLAG nanocluster samples with different capping layer materials: capping layer thickness (θ), spin block size N obtained by fitting the magnetization curves using Eqs. (2) and (3), orbital-spin moment ratio ($\frac{\mu_L}{(\mu_S+7\mu_T)}$), and magnetic anisotropy are reported.

Sample	θ (nm)	N (atoms)	$\frac{\mu_L}{(\mu_S+7\mu_T)}$	R_{L_3} anisotropy	Orbital moment anisotropy
Al ₂ O ₃	3	26	(0.38±0.05)	None	
Pt	2	23		None	
Au	5	21		None	
MnPt	1	17	(0.37±0.05)	In-plane	In-plane
MnPt	3			None	Polar

In Fig. 5(a), a plot of Co R_{L_3} versus magnetic field is shown for the samples capped with non-magnetic materials Au, Pt, and Al₂O₃, measured at $T = 15$ K both for $\vartheta = 0^\circ$ and 70° . In all the three cases, the highest available magnetic field was almost sufficient to saturate the Co magnetization. However, the ratios R_{L_3} at $B = 5$ T for the three samples differ: the highest value of $R_{L_3} = 0.6$ is found for Al₂O₃ capping, which is slightly enhanced compared to the values found for large clusters in Sec. III A. This value is in line with other experimental data for Al₂O₃ capped Co clusters.²¹ The sample capped with Au has a strongly reduced signal of only $R_{L_3} = 0.3$. As commented at the end of Sec. II for 2-dimensional 3d metal clusters like those fabricated by BLAG, the ratio R_{L_3} can be strongly affected by orbital L_z and spin-dipole operator T_z contributions. $\langle T_z \rangle$ values are known to be large and negative for Co monolayers in contact with Au and Pt surfaces. According to DFT calculations for extended 2-dimensional Co clusters on Au(111) systems, we expect R_{L_3} to be reduced by $\sim -25\%$ due to T_z contributions, while the actual Co spin moment $\langle \mu_S \rangle$ remains unaffected.²⁰ If we compare the reduced $R_{L_3} = 0.3$ found for Au capping with the $R_{L_3} = 0.5$ found for bulk-like clusters with a spin moment of $\mu_S \sim 1.6\mu_B$ and assume a reduction of $\sim -25\%$ due to T_z contributions in the case of Au capping, then we get an estimation of the spin moment of $\mu_S \sim 1.4\mu_B$. The fact that we see lower spin moments than predicted by DFT theory is consistent with the earlier experimental findings on similarly fabricated BLAG Co clusters in contact with Ag(111). In this case, DFT predicts negligible T_z contributions, partly because Ag is a lighter element with less spin-orbit coupling contributions. There are several possible reasons for this discrepancy, which we describe in Ref. 25 in detail; however, this is not in the focus of the present work. Finally, the sample capped with Pt has an intermediate saturation value $R_{L_3} = 0.45$. In the case of Pt, we saw partial oxidation, possibly due to an insufficient capping thickness: the XAS line shape shows typical features of a Co and CoO mixture (not shown). Partial oxidation should lead to reduced R_{L_3} values.²²

The orbital moments μ_L of BLAG clusters are expected to be larger than those of deposited clusters due to a smaller dimension and therefore a reduced number of Co neighbors. For the clusters capped with weakly interacting Al₂O₃, we indeed find an orbital-spin moment ratio of (0.38±0.05), 3–4 times larger than that of large deposited clusters in

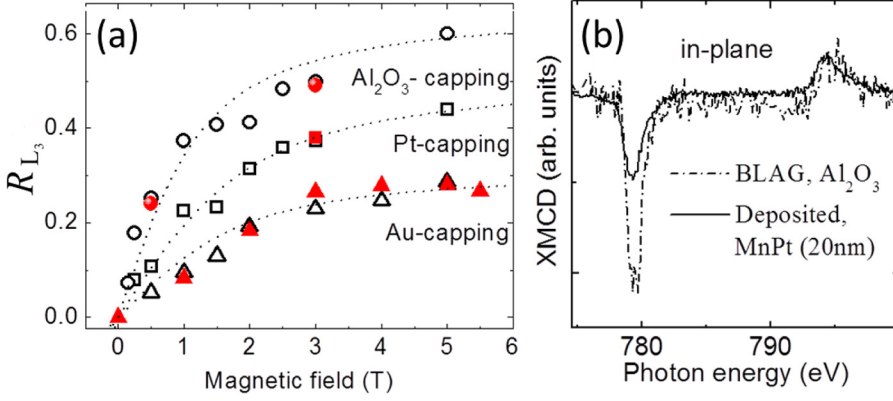


FIG. 5. (a) Co R_{L_3} versus magnetic field for BLAG cluster capped with Al_2O_3 , Pt, and Au. Open (filled) circles refer to $\vartheta = 0^\circ$ ($\vartheta = 70^\circ$) geometry both at $T = 15$ K. The dotted lines are fits to the data using Eqs. (2) and (3). (b) XMCD spectra of Al_2O_3 and MnPt (from Sec. III A) capped samples normalized to each other at the L_2 absorption edge.

Sec. III A. Also, the comparison by normalizing the XMCD signal at the L_2 edge (see Fig. 5(b)) supports this trend.

A common feature to all three samples is the absence of remanence ($R_{L_3} = 0$ at $B = 0$). The Co clusters, therefore, must have a blocking temperature T_b^{Co} below the measurement temperature of $T = 15$ K. A general estimation for the blocking temperature, considering the measuring time of our experiments, is given by the following formula:²³

$$T_b = \frac{N \cdot \Delta E}{27 \cdot k_B}, \quad (1)$$

where ΔE is the effective anisotropy energy per atom and k_B is the Boltzmann constant. Using $N = 100$ as an upper estimation for the number of atoms per Co cluster found by scanning tunneling microscopy (STM) measurements,²⁴ we get $\Delta E \leq 0.3$ meV in order to have $T_b^{\text{Co}} \leq 15$ K. Magnetocrystalline anisotropy energy (MAE) in $3d$ elements is caused by anisotropic $3d$ state configurations, which are triggered by electronic interactions with a symmetry-breaking environment. In our case, this is caused by lateral intracluster Co-Co bonding but also by the capping material. Since for non-magnetic capping we do not observe any anisotropy between $\vartheta = 0^\circ$ and 70° , we expect this interaction to be rather weak and maybe also not homogeneous due to disorder in the capping layer.³¹

In the superparamagnetic limit, one can fit the magnetization curves using a classical Boltzmann statistics of a macrospin $\mathbf{m}_N = N \cdot \mu_S$ in a magnetic field. The fit results shown in Fig. 5(a) are obtained using the formula

$$R_{L_3}(\mathbf{m}_N, \mathbf{H}) = R_{\text{sat}} \int (\hat{\mathbf{m}} \cdot \hat{\mathbf{h}}) e^{-E(\mathbf{m}_N, \mathbf{H})/k_B T} d\Omega / Z, \quad (2)$$

$$E(\mathbf{m}_N, \mathbf{H}) = -(\mathbf{m}_N \cdot \mathbf{H}) - N \cdot E_A (\hat{\mathbf{m}} \cdot \hat{\mathbf{n}})^2, \quad (3)$$

where R_{sat} is the saturation value of the XMCD/XAS ratio R_{L_3} , $\hat{\mathbf{m}}$ the unit vector of the macrospin moment, and $\mathbf{H} = H \cdot \hat{\mathbf{h}}$ the magnetic field vector. E_A is the magnetic anisotropy energy per atom with an uniaxial direction $\hat{\mathbf{n}}$. Z is the partition function for states $\hat{\mathbf{m}}$ on the unit sphere Ω . For the non-magnetic capping, the value E_A was set to zero since polar and in-plane measurements in Fig. 5(a) show similar results. Assuming a bulk hcp spin moment of $\mu_S = 1.6\mu_B$ per Co atom,¹² the spin block size found for Al_2O_3 capping is $N = 26$. This number is at the lower edge of the size

distribution interval of 20 to 100 atoms given by careful STM measurements.²⁴ For the Au capped sample, we find $N = 21$ for the above discussed reduced spin moment of $\mu_S = 1.4\mu_B$ per atom.

2. MnPt capping

The MnPt staircase wedge was deposited at low temperatures ($T \sim 50$ K) in order to impede thermal diffusion of the atoms impinging the substrate and to favor the formation of a continuous, chemically disordered capping layer. The Mn $L_{3,2}$ XAS for $\vartheta = 0^\circ$ and 70° is shown in Fig. 4(b) for the two extreme positions of the wedge, $\theta_{\text{MnPt}} = 1$ nm and 3 nm. The agreement with the simulated XAS for a Mn(2^+) ion in O_h symmetry ($10Dq = 0.6$ eV) again suggests at least local $L1_0$ ordering of MnPt. However, in contrast to the room temperature grown MnPt films in Sec. III A, only a small anisotropy in the XAS spectra between $\vartheta = 0^\circ$ and 70° is visible. We attribute this to increased disorder during low temperature growth. As we show below, this does not significantly influence the formation of the AFM state at larger MnPt coverages.

XAS and XMCD spectra measured at $T = 15$ K are shown in Fig. 6 for both Co and Mn, and for three positions along the wedge. The measurements were done after FC at $B = +5$ T, $\vartheta = 70^\circ$. Corresponding magnetization curves at the extreme positions $\theta_{\text{MnPt}} = 1$ nm and 3 nm of the wedge are shown in Figs. 7(a) and 7(b). The main results are:

(1) *Thin MnPt capping* ($\theta_{\text{MnPt}} \leq 1$ nm): the Co magnetization is saturated at $R_{L_3} \sim 0.6$ very similar to what is found for non-magnetic capping Al_2O_3 . Also similar to the latter sample, the orbital-spin ratio has a relatively large value of (0.37 ± 0.05) . However, in contrast to non-magnetic capping there is a preferential in-plane magnetic direction visible in the R_{L_3} signal of Co. Using Eqs. (2) and (3), we can fit the Co data in Fig. 7(a) for both directions with a macrospin $m_N = 27\mu_B$ (e.g., $N = 17$ and spin moment $\mu_S = 1.6\mu_B$ per Co atom if we disregard contributions from exchange coupled Mn moments, see discussion below) and $E_A = (-0.16 \pm 0.03)$ meV (with the hard axis $\hat{\mathbf{n}}$ oriented perpendicular to the sample normal).

The average Mn magnetization is not saturated but the value $R_{L_3} \sim 0.4$ is large at $\vartheta = 70^\circ$ and its anisotropy is even stronger than that of Co. From the insets in Figs. 6(a) and 6(d), one notices that also the orbital moment at $\vartheta = 70^\circ$ is larger compared to $\theta = 0^\circ$ both for Co and Mn.

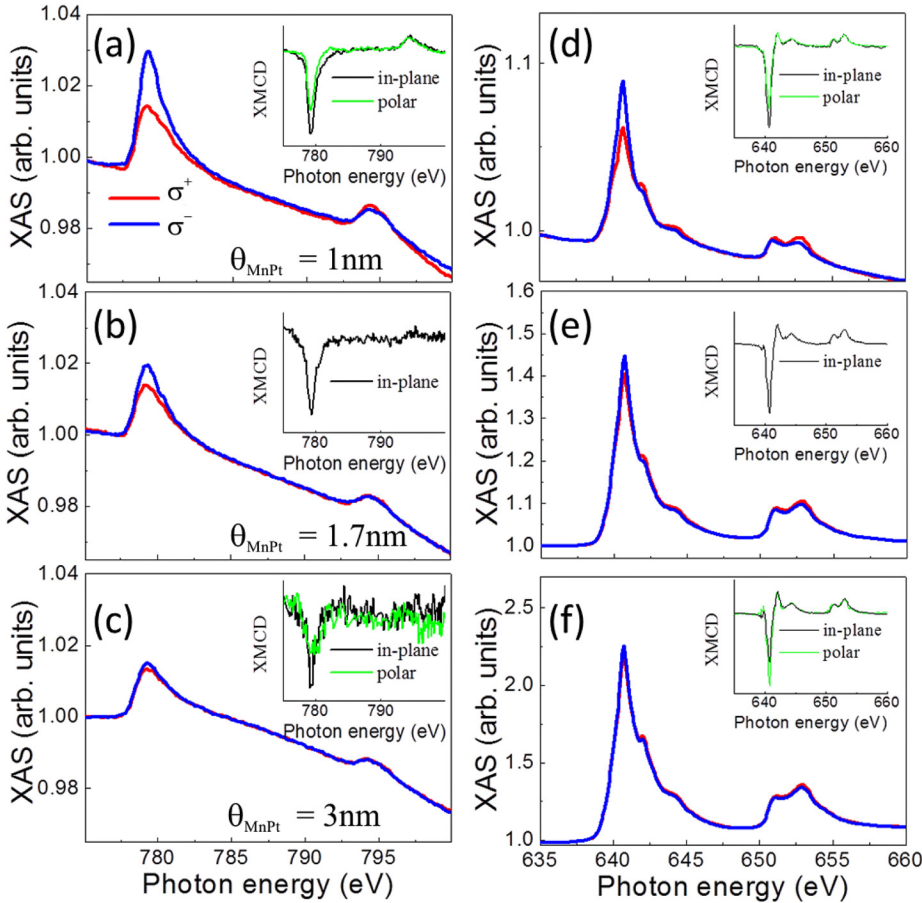


FIG. 6. XAS (σ^+ , σ^-) (red and blue lines) for BLAG nanocluster capped with increasing MnPt thickness. The figure shows Co (a)-(c) and Mn (d)-(f) spectra at $\vartheta = 70^\circ$, $B = 5$ T, and $T = 15$ K. The insets show XMCD spectra for $\vartheta = 0^\circ$ and $\vartheta = 70^\circ$ normalized at the L_2 absorption edge.

(2) *Thicker MnPt capping* ($1 \text{ nm} < \theta_{\text{MnPt}} \leq 3 \text{ nm}$): It is evident from Figs. 6(a)-6(c) and 7(c) that with increasing θ_{MnPt} the Co dichroism is significantly reduced by up to a factor of 6 compared to the value found at thin MnPt cappings; accordingly, the magnetization curves in Fig. 7(a) are not saturated at $B = 5$ T for $\theta_{\text{MnPt}} = 3 \text{ nm}$. Both Co R_{L_3} and orbital moment still show in-plane anisotropy but the signal-to-noise ratio is already quite poor. Also, the average

Mn magnetization is progressively quenched and—at $\theta_{\text{MnPt}} = 3 \text{ nm}$ —becomes about 7 times smaller compared to thin capping layers. For this high coverage, there appears to be no anisotropy in the Mn R_{L_3} signal, although the anisotropy in the orbital moment shown in the inset of Fig. 6(f) suggests a polar easy axis direction.

(3) In all cases, no remanence and hence no EB is observed.

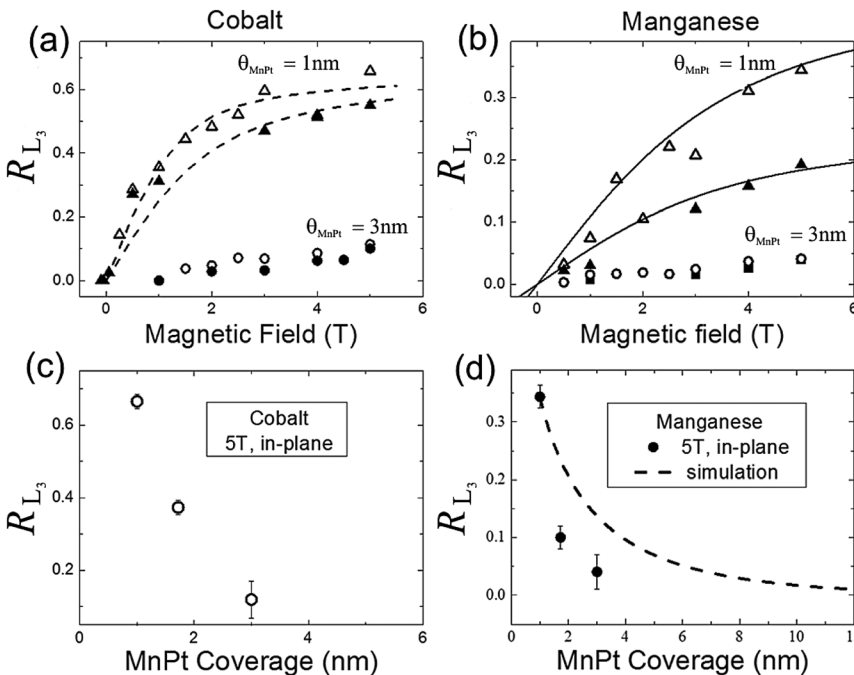


FIG. 7. Magnetization curves at $T = 15$ K in the two extreme points of the wedge $\theta_{\text{MnPt}} = 1 \text{ nm}$ and 3 nm (triangular and circular symbols, respectively) for Co (a) and Mn (b). Open (filled) symbols refer to $\vartheta = 70^\circ$ ($\vartheta = 0^\circ$) geometry. The sample was FC at $B = +5$ T, $\vartheta = 70^\circ$. Dashed lines in (a) are fits using Eqs. (2) and (3), while full lines in (b) are guides to the eye. (c) and (d) show Co and Mn R_{L_3} values at $B = 5$ T versus MnPt coverage, respectively. The dashed line in (d) shows the expected decrease of Mn R_{L_3} with coverage assuming a constant moment for Mn-I at the interface to the Co cluster. The simulation uses the model in Ref. 17 for the exponential decay of the XAS signal.

Unlike in the case of the large clusters in Sec. III A, for BLAG samples the clusters form a dense array on the h-BN covering a large area of approximately 70% of the surface and the XMCD technique captures a considerably enhanced fraction of Mn atoms at the interface with Co clusters (compare STM images (a) and (b) in Fig. 1). Thus, in the thin part of the wedge ($\theta_{\text{MnPt}} = 1$ nm), one is sensing Mn atoms in the vicinity of this interface, called Mn-I hereafter. On the other hand, for higher values of the MnPt thickness, the measured XMCD also reflects the magnetization of Mn within the bulk MnPt phase (Mn-II). From the trend of Mn magnetization versus MnPt thickness in Fig. 7(d), one can see that the average unsaturated Mn-I magnetization at the interface is much higher than that of magnetically compensated MnPt capping of 20 nm thickness. In fact, at $\theta_{\text{MnPt}} = 1$ nm, we measure $R_{L_3} \sim 0.35$ along the in-plane easy axis direction, which is 70% of the value $R_{L_3} \sim 0.5$ of Mn in FM MnPt₃.²⁹ Taking into account that at $B = 5$ T our measured R_{L_3} is far from saturation we believe that $\langle \mu_S^{\text{Mn-I}} \rangle$ is most likely comparable to the value $\mu^{\text{MnPt}_3} = 3.9\mu_B$ in MnPt₃.^{40,41} In agreement with the observation in Sec. III A, on large deposited clusters a compensated AFM phase only develops at larger MnPt thicknesses $\theta_{\text{MnPt}} > 3$ nm. However, surprisingly in the case of small BLAG Co systems a new effect occurs. With the formation of a bulk AFM state, a strong quenching of the average magnetization of the Co clusters is observed. Possible physical mechanisms behind this effect are:

- (i) *Chemical coordination*: Co atoms can have reduced spin moments due to the degree and quality of coordination with the MnPt environment. The extreme case of diffusion of single Co atoms into the MnPt matrix, however, can be ruled out, since alloying processes start at temperatures above $T \sim 200$ °C.⁵ Against the importance of coordination between Co cluster and MnPt speaks, the fact that at $\theta_{\text{MnPt}} = 1$ nm, a thickness ~ 5 times larger than the monatomic cluster height, Co still has a high value R_{L_3} of the order of what is found for the weakly interacting capping case of Al₂O₃. A reason for the weak influence of chemical coordination with MnPt could be the relatively strong localization of Mn 3d states in MnPt.^{37,38}
- (ii) *Indirect RKKY coupling*: RKKY interaction between clusters mediated by the metallic MnPt capping layer can lead to AFM coupling, quenching the measured average Co moments. Such an effect was observed, e.g., in Co clusters capped with Cu layers (see Ref. 26). Here, however, calculations predict the RKKY coupling energy to be only of the order of 0.05 meV for Co clusters with $N \sim 20$,²⁷ competing with the much larger Zeeman energy of about 10 meV for each macrospin at $B = 5$ T. Moreover, as discussed in (i), the hybridization between Co 3d and MnPt states necessary for RKKY coupling seems to be inefficient in our systems. Therefore, RKKY interactions are considered unimportant.
- (iii) *Direct exchange coupling at the interface*: The overall magnetic interaction between Co clusters and AFM domains in the MnPt matrix is defined by the local

exchange coupling constants J_{int} between Mn and Co spins at the cluster interface. Strong correlations between the Co and Mn magnetization behavior visible in Figs. 7(a) and 7(b) suggest that this interaction plays an important role. First, we see a significant magnetic anisotropy in the Co signal when thin MnPt capping is used, while for non-magnetic capping materials (see Fig. 5) no anisotropy is visible. MnPt is expected to have a large magnetic anisotropy energy ΔE per atom (see, e.g., Ref. 36 and references therein), and the fact that we observe the in-plane easy axis both in Mn and Co strongly supports the idea that MnPt transfers its magnetic anisotropy to the Co clusters via J_{int} . Second, a very similar dependence of the magnetization values of Mn and Co at $B = 5$ T is observed with increasing θ_{MnPt} (see Figs. 7(c) and 7(d)), which again suggests the importance of exchange coupling via the interface.

According to the above arguments, the experimentally observed quenching of the average Co cluster magnetization will be discussed in terms of direct exchange coupling at the interface with MnPt.

The most straightforward interpretation would be a forced AFM order of Co spins within each cluster under the influence of the direct exchange coupling with the AFM MnPt phase. For this, a strong Mn-Co interface exchange interaction and firm Mn-Mn AFM coupling would be required, able to overcome the intracluster Co-Co FM order. Such a scenario is sketched in Fig. 8(b), upper panel, where the Co spins follow the Mn spins at the interface with the

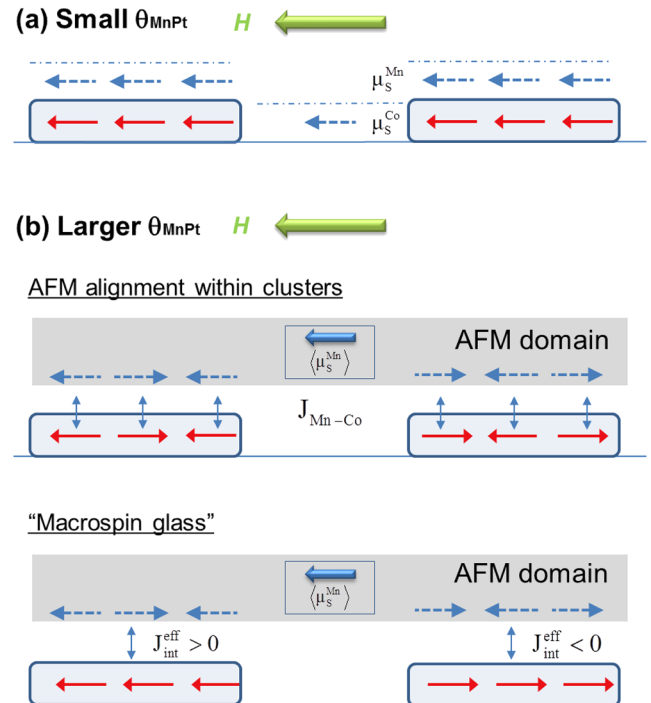


FIG. 8. Proposed model for the magnetic coupling between Co clusters and MnPt for (a) ultrathin layers ($\theta_{\text{MnPt}} = 1$ nm) and (b) $\theta_{\text{MnPt}} = 3$ nm. In (b), the low average Co magnetization is modeled by either an induced AFM alignment within each cluster or random orientation of macrospins with respect to each other (“macrospin-glass”) as explained in the text.

MnPt matrix and form an intrinsically spin-compensated magnetic structure within each cluster. Using $N = 17$ for the number of atoms in each macrospin (see Table II) we can fit the data in Fig. 7(a) at $\theta_{\text{MnPt}} = 3\text{nm}$ according to Eqs. (2) and (3). The result is a very small average spin moment per Co atom of $\langle\mu_S\rangle = 0.1\mu_B$ in a cluster with vanishing anisotropy energy $E_A = 0$. In this scenario, the formation of a stable AFM phase in MnPt at higher θ_{MnPt} drives each Co macrospin separately into a spin-compensated structure, which leads to very small average values R_{L_3} for Co. Moreover, the Zeeman Term $\mathbf{m}_N \cdot \mathbf{H}$ is strongly reduced, which would explain the linear magnetization curve up to $B = 5\text{ T}$ and the absence of saturation.

We believe, however, that the interpretation of the results is more complex. Since the intrinsic exchange coupling J_{Co} between Co moments within a monolayer cluster is large (J_{Co} in free monolayer clusters is predicted to be of the order of 1 eV,³⁹ while the AFM exchange coupling in stoichiometric bulk MnPt is between $J_{\text{Mn}} = 10 - 100\text{ meV}$ (Refs. 36 and 38)), one expects that the macrospin $N \cdot \mu_S$ of each Co cluster will be preserved for all MnPt capping thicknesses. The quenching of the average magnetization of the ensemble of cluster macrospins with increasing MnPt thickness then has to be sought in a more complex magnetic interaction with MnPt capping layer. In the following, we assume that the Co macrospins preserve their intrinsic FM structure, which at higher θ_{MnPt} compulsory demands for a large average misalignment of the macrospins with respect to each other in order to explain the observed low R_{L_3} values. Such misalignments could be triggered by the formation of AFM domains in the MnPt capping layer due to structural and chemical disorders (DS model).

With the aim to better understand the role of the DS model in our system, we now discuss in more detail possible interface magnetic coupling scenarios between Co clusters and Mn moments at small and large MnPt coverages. We start with the description of the system at low MnPt coverage. First of all, we notice the fact that independent of θ_{MnPt} neither Mn nor Co shows remanence at the measuring temperature of $T = 15\text{ K}$. Further, if we use the superparamagnetic picture of magnetically independent Co macrospins, but each rigidly exchange coupled to a certain MnPt volume $V_{\text{MnPt}}^{\text{Ex}}$, the experimental finding $T_b < 15\text{ K}$ refers to the composite cluster including $V_{\text{MnPt}}^{\text{Ex}}$, which effectively increases the block size N and changes the effective anisotropy energy ΔE in Eq. (1). According to the literature L1₀, MnPt reaches large MAE densities up to $K_{\text{MnPt}} \sim 10^5\text{ erg/cm}^3$, which can dominate the blocking behavior of the cluster. We can estimate an upper limit for the exchanged coupled MnPt volume if we set $27 \cdot k_B T \geq V_{\text{MnPt}}^{\text{Ex}} \cdot K_{\text{MnPt}}$, $k_B T$ being the available thermal energy at $T = 15\text{ K}$, and get $V_{\text{MnPt}}^{\text{Ex}} \leq (8\text{ nm})^3$. The order of magnitude of the upper limit volume is in line with the polycrystalline structure observed in TEM. However, we want to stress that according to the DS model, a crystalline grain volume of this size might be subdivided into smaller independent AFM domains due to chemical disorder in the L1₀ structure, which would reduce the rigidly exchange coupled volume $V_{\text{MnPt}}^{\text{Ex}}$. Indeed, for $\theta_{\text{MnPt}} = 1\text{ nm}$, the successful fitting of the magnetization curves in Fig. 7(a) with a macrospin

$m_N = 27\mu_B$ similar to the case of non-magnetic capping ($m_N = 27\mu_B$ corresponds to $N = 17$ and $\mu_S = 1.6\mu_B$ per Co atom) is in favor of a rather small $V_{\text{MnPt}}^{\text{Ex}}$ since including a larger number N_{Mn} of FM or AFM coupled finite type Mn-I moments $\langle\mu_S^{\text{Mn-I}}\rangle$ would drastically change the estimation of the Co block size N_{Co} . From the slight reduction of N (see Table II) compared to the non-magnetic capping samples, one would estimate a FM coupling of at most $N_{\text{Mn}} \sim 4$ atoms with $\langle\mu_S^{\text{Mn-I}}\rangle \sim \mu^{\text{MnPt}_3} = 3.9\mu_B$ to form a total macrospin $m_{\text{tot}} = N_{\text{Co}}\mu_S^{\text{Co}} + N_{\text{Mn}}\mu^{\text{MnPt}_3}$ (see Fig. 8(a) for model principle). The FM coupling is supported by the fact that the Mn R_{L_3} signal always shows the same sign as that of Co.

While the superparamagnetic picture of independent Co macrospins each exchanged coupled to a certain volume with Mn-I type moments would be a realistic model for small θ_{MnPt} , it fails to describe the magnetization curves at $\theta_{\text{MnPt}} = 3\text{ nm}$ in Fig. 7(a). In the large thickness regime, we suggest misalignment effects of macrospins to play the key role. At this point, we want to come back to the DS model by Morel *et al.*,⁴ which states that magnetic properties like the EB effect of Co clusters embedded in bulk MnPt are correlated to the bulk magnetization M_{MnPt} . In the R_{L_3} data of Figs. 7(a) and 7(b), we see a similar behavior, which underlines the importance of Mn-II moments with respect to Mn-I and the appearance of the DS for large enough MnPt thicknesses.

To test this interpretation, the decrease of the Mn magnetization is simulated considering the escape depth λ_e of electrons within the capping layer. In Fig. 7(d), the decay of the Mn R_{L_3} signal versus MnPt coverage is estimated (dashed line) for a system containing both species Mn-I and Mn-II. Mn-I is fixed at the origin ($x = 0$) and its R_{L_3} value is assumed constant with increasing MnPt coverage. We then consider x layers of MnPt containing only Mn-II type and assume for them a perfectly AFM phase with $R_{L_3} = 0$. The simulated signal $R_{L_3}(\theta_{\text{MnPt}})$ is obtained by averaging the two species and considering the respective exponential decays due to λ_e . From this simulation, it appears that the decrease of Mn magnetization cannot be explained in a simple way by the exponential decay of a constant signal arising from interfacial Mn-I, as this would lead to a curve with significantly reduced steepness. Instead, it seems that the Mn-I species has a progressively quenched average moment, due to formation of the AFM phase. At the same time, the Co magnetization is also quenched and the decay with MnPt coverage is very similar to that of Mn (Figs. 7(c) and 7(d)).

Our conclusion is that at low MnPt coverages, where the AFM phase between Mn spins is not stabilized, the Co clusters of $N \approx 20$ are intrinsically FM coupled and behave like superparamagnetic particles with a slightly enhanced macrospin due to a few FM aligned Mn-I type spins at the interface (see Fig. 8(a)). At larger MnPt coverages where the AFM DS is fully developed, type Mn-I spins at the interface in average become antiferromagnetically aligned with respect to each other, following the AFM bulk-like DS with a low residual magnetization M_{MnPt} . In average, the Co macrospins m_N now follow the trend of the MnPt magnetization, $\langle m_N \rangle \sim M_{\text{MnPt}}$, which we interpret as random orientation of macrospins with respect to each other (“macrospin-glass”) under the influence

of the DS (see Fig. 8(b), lower panel): if a larger number of macrospins are coupled to an extended AFM MnPt domain (with a small residual moment $\langle \mu_S^{\text{Mn}} \rangle$) via a distribution of positive and negative effective exchange couplings, the average macrospin $\langle m_N \rangle$ can be reduced. The effective exchange coupling constants of the macrospins, $J_{\text{int}}^{\text{eff}}$, will be dependent on the local orientation of the Mn-I spins at the respective cluster interfaces.

IV. SUMMARY AND CONCLUSIONS

The exchange bias behavior of 2-dimensional cobalt nanocluster arrays in contact with thin antiferromagnetic MnPt capping layers is studied. The goal is to test the domain state model for exchange bias in reduced dimensions. Capping with magnetic MnPt layers has a profound effect on the cluster magnetization: a progressive quenching of the average Co magnetization by up to a factor 6 is observed while increasing the MnPt thickness. We explain this significant effect to be due to the exchange coupling between Co and Mn spins at the interface. For low MnPt thicknesses, the antiferromagnetic phase is not stable and the Mn spins at the interface follow the superparamagnetic behavior of the Co clusters. As the antiferromagnetic phase in MnPt develops with increasing MnPt thickness, we propose that either (i) a spin-compensated magnetic structure within each Co cluster is formed or (ii) Co macrospins with intrinsic ferromagnetic coupling are randomly oriented with respect to each other (“macrospin-glass” model) both leading to a very low average magnetization. This effect is only observed in reduced cluster dimensions. For larger 3-dimensional nanoclusters of $\sim 5\text{nm}$ in diameter with blocking temperatures well above the measuring temperature, the prototypical exchange bias behavior is recovered with an average Co magnetization corresponding to a bulk ferromagnetic phase. Here, we could show that layer thicknesses can be reduced to dimensions of the nanoclusters itself without losing exchange bias behavior.

ACKNOWLEDGMENTS

We acknowledge the Stuttgart Center for Electron Microscopy (StEM) and P. Kopold for the TEM images. We thank N. B. Brookes for valuable input.

¹R. L. Stamps, *J. Phys. D: Appl. Phys.* **33**, R247 (2000).

²M. Kiwi, *J. Magn. Magn. Mater.* **234**, 584 (2001).

³U. Nowak, K. D. Usadel, J. Keller, P. Miltsenyi, B. Beschoten, and G. Güntherodt, *Phys. Rev. B* **66**, 014430 (2002).

⁴R. Morel, C. Portemont, A. Brenac, and L. Notin, *Phys. Rev. Lett.* **97**, 127203 (2006).

⁵E. H. Morales, Y. Wang, D. Lederman, A. J. Kellock, and M. J. Carey, *J. Appl. Phys.* **93**, 4729 (2003).

⁶A. Lodi Rizzini, C. Krull, Balashov, A. Mugarza, C. Nistor, F. Yakhov, V. Sessi, S. Klyatskaya, M. Ruben, S. Stepanow, and P. Gambardella, *Nano Lett.* **12**, 5703 (2012).

⁷M. Corso, W. Auwarter, M. Muntwiler, A. Tamai, T. Greber, and J. Osterwalder, *Science* **303**, 217 (2004).

⁸S. Berner, M. Corso, R. Widmer, O. Groening, R. Laskowski, P. Blaha, K. Schwarz, A. Goriachko, H. Over, S. Gsell, M. Schreck, H. Sachdev, T. Greber, and J. Osterwalder, *Angew. Chem., Int. Ed.* **46**, 5115 (2007).

⁹S. Gsell, M. Fischer, M. Schreck, and B. Stritzker, *J. Cryst. Growth* **311**, 3731 (2009).

¹⁰I. Brihuega, C. H. Michaelis, J. Zhang, S. Bose, V. Sessi, J. Honolka, M. A. Schneider, A. Enders, and K. Kern, *Surf. Sci.* **602**, L95 (2008).

¹¹Co: 778eV ($L_{3\text{-edge}}$) and 773eV (L_3 pre-edge); Mn: 640eV ($L_{3\text{-edge}}$) and 635eV (L_3 pre-edge).

¹²C. T. Chen, Y. U. Idzerda, H. J. Lin, N. V. Smith, G. Meigs, E. Chaban, G. H. Ho, E. Pellegrin, and F. Sette, *Phys. Rev. Lett.* **75**, 152 (1995).

¹³The curves have been obtained following the model in Ref. 17 with $\lambda_e = 50 \text{ \AA}$. $\lambda_e = 20 \text{ \AA}$ would lead to a better agreement with our experiment; however, from our experimental data, the intensity attenuation of the $L_{3,2}$ edges of Co versus MnPt coverage is still quite small for the sample with $\theta_{\text{MnPt}} = 5 \text{ nm}$, therefore it is reasonable to expect a larger λ_e .

¹⁴E. Stavitski and F. M. F. de Groot, *Micron* **41**, 687 (2010).

¹⁵J. Fujii, F. Borgatti, G. Panaccione, M. Hochstrasser, F. Maccherozzi, G. Rossi, and G. van der Laan, *Phys. Rev. B* **73**, 214444 (2006).

¹⁶B. Wang and M.-L. Bocquet, *J. Phys. Chem. Lett.* **2**, 2341 (2011).

¹⁷R. G. Jones and D. P. Woodruff, *Surf. Sci.* **114**, 38–46 (1982).

¹⁸J. Zhang, V. Sessi, C. H. Michaelis, I. Brihuega, J. Honolka, K. Kern, R. Skomski, X. Chen, G. Rojas, and A. Enders, *Phys. Rev. B* **78**, 165430 (2008).

¹⁹G. van der Laan, *Phys. Rev. B* **55**, 8086 (1997).

²⁰O. Šipr, J. Minar, and H. Ebert, *Europhys. Lett.* **87**, 67007 (2009).

²¹F. Luis, F. Bartolome, F. Petro, J. Bartolome, L. M. Garcia, C. Deranlot, H. Jares, M. J. Martinez, P. Bencok, F. Wilhelm, A. Rogalev, and N. B. Brookes, *Europhys. Lett.* **76**, 142 (2006).

²²P. Imperia, P. Andrezza, D. Schmitz, J. Penuelas, and C. Andrezza-Vignolle, *J. Magn. Magn. Mater.* **310**, 2417 (2007).

²³Here, we use $T_b = \frac{N \cdot \Delta E}{\ln(\tau_m/\tau_0) \cdot k_B}$ with $\tau_m = 60\text{s}$ and $\tau_0 = 10^{-10}\text{s}$ being the typical measuring and relaxation times, respectively.

²⁴C. H. Michaelis, Ph.D. dissertation, University of Konstanz (2009).

²⁵V. Sessi, K. Kuhnke, J. Honolka, A. Enders, J. Zhang, P. Bencok, S. Bornemann, and K. Kern, *Phys. Rev. B* **81**, 195403 (2010).

²⁶D. A. Eastham, Y. Qiang, T. H. Maddock, J. Kraft, J.-P. Schille, G. S. Thompson, and H. Haberland, *J. Phys.: Condens. Matter* **9**, L497 (1997).

²⁷D. Altbir, *Phys. Rev. B* **54**, R6823 (1996).

²⁸S. Honda, M. Nawate, and T. Norikane, *J. Magn. Magn. Mater.* **220**, 85 (2000).

²⁹T. Kato, Y. Fujiwara, S. Iwata, and S. Tsunashima, *J. Magn. Magn. Mater.* **240**, 517 (2002).

³⁰T. Sato, M. Tsunoda, and M. Takahashi, *J. Magn. Magn. Mater.* **240**, 277 (2002).

³¹Even in an asperomagnetic system with random distribution of local uniaxial hard axis directions \hat{n} with MAEs larger than $\Delta E \sim 0.3 \text{ meV}$, the remanence should remain finite.

³²H. J. Lee, G. Kim, D. H. Kim, J.-S. Kang, C. L. Zhang, S.-W. Cheong, J. H. Shim, S. Lee, H. Lee, J.-Y. Kim, B. H. Kim, and B. I. Min, *J. Phys.: Condens. Matter* **20**, 295203 (2008).

³³K. Takano, R. H. Kodama, A. E. Berkowitz, W. Cao, and G. Thomas, *Phys. Rev. Lett.* **79**, 1130 (1997).

³⁴A. Goriachko, Y. B. He, and H. Over, *J. Phys. Chem. C* **112**, 8147–8152 (2008).

³⁵R. Morel, A. Brenac, P. Bayle-Guillemaud, C. Portemont, and F. La Rizza, *Eur. Phys. J. D* **24**, 287 (2003).

³⁶P. Ravindran, A. Kjekshus, H. Fjellvåg, P. James, L. Nordström, B. Johansson, and O. Eriksson, *Phys. Rev. B* **63**, 144409 (2001).

³⁷S. Imada, T. Muro, T. Shishidou, S. Suga, H. Maruyama, K. Kobayashi, H. Yamazaki, and T. Kanomata, *Phys. Rev. B* **59**, 8752 (1999).

³⁸R. Y. Umetsu, K. Fukamichi, and A. Sakuma, *J. Appl. Phys.* **91**, 8873 (2002).

³⁹T. O. Strandberg, C. M. Canali, and A. H. MacDonald *Phys. Rev. B* **73**, 144415 (2006).

⁴⁰K. W. Wierman and R. D. Kirby, *J. Magn. Magn. Mater.* **154**, 12 (1996).

⁴¹M. Rickart, A. Guedes, B. Negulescu, J. Ventura, J. B. Sousa, P. Diaz, M. MacKenzie, J. N. Chapman, and P. P. Freitas, *Eur. Phys. J. B* **45**, 207 (2005).